Original Article

POROUS IRON SCAFFOLDS WITH THE ADDITION OF MANGANESE AND COPPER—PHYSICOCHEMICAL CHARACTERISTICS AND BIOCOMPATIBILITY ANALYSIS

M. Grodzicka[1], G. Gąsior[1], T. Jędrzejewski[2], S. Wrotek[2], P. Madajski[1] and A. Radtke[1,*]

[1]Faculty of Chemistry, Nicolaus Copernicus University in Toruń, 87-100 Toruń, Poland
[2]Faculty of Biological and Veterinary Sciences, Nicolaus Copernicus University in Toruń, 87-100 Toruń, Poland

Abstract

Background: Biodegradable iron scaffolds are potential biomaterials which can be used for the needs of modern cardiology. The primary criterion for biodegradable implants is corrosion time, and pure iron has a relatively low corrosion rate in the physiological environment, which can be a limitation for materials that require faster biodegradation. The introduction of manganese (Mn) and copper (Cu) as alloying elements into iron could increase the corrosion rate through changes in the microstructure and electrochemical potentials of the material. **Methods**: The materials investigated in this study were pure iron scaffolds ferrite (Fe) and scaffolds with the addition of manganese (35 % w/w) and copper (1 % w/w): Fe35Mn, Fe1Cu, and Fe35Mn1Cu, subsequently referred to as Fe, FeMn, FeCu, and FeMnCu, respectively. They were obtained by applying the template method and sintering procedure, using the polyurethane (PU) and melamine (Mel) polymeric templates. Samples have been characterized in terms of their structure and morphology. Their electrochemical corrosion has been carried out with the use of potentiodynamic polarization. The biological *in vitro* studies were conducted using four cell lines: human aortic smooth muscle cells (HASMC), human umbilical vein endothelial cells (HUVEC), murine fibroblasts (L929), and murine macrophages (RAW 264.7). **Results**: Depending on the template used, we obtained iron scaffolds with larger pores and higher porosity for the PU template (0.7–1.6 mm, porosity 97 %) and smaller pores with lower porosity for the Mel template (0.1–0.35 mm, porosity 21 %). Additives of manganese (35 wt %) and copper (1 wt %) in the samples result in differences in orphology and composition. Analysis of the polarisation curves clearly indicates that the type of alloy used significantly determines the degradation of the scaffold, while the type of scaffold used (PU-based or Mel-based) has less influence. FeMn-Mel scaffolds exhibited E_{corr} = −475.5 mV and I_{corr} = 11.5 μA, FeMnCu-Mel E_{corr} = −443.5 mV and I_{corr} = 8.67 μA, while FeCu-Mel showed E_{corr} = −369.4 mV and I_{corr} = 8.11 μA. Among PU-based samples, FeMn-PU showed E_{corr} = −576.6 mV and I_{corr} = 9.44 μA, FeMnCu-PU E_{corr} = −526.8 mV and I_{corr} = 7.56 μA, whereas FeCu-PU reached E_{corr} = −479.2 mV and I_{corr} = 19.61 μA. When comparing the toxic effects of scaffolds based on polyurethane and melamine, all materials made based on a melamine template are less toxic to HASMC, HUVEC, and L929 cells than their polyurethane-based counterparts. **Conclusions**: Considering the impact on the viability of key cells essential for the proper implantation of cardiovascular devices, such as endothelial cells, aortic smooth muscle cells, and fibroblasts, as well as the assessment of potential inflammatory induction, melamine-based scaffolds containing Mn or Cu demonstrate the greatest application potential. Additionally, these materials also show significant anti-inflammatory effects, further supporting their suitability for use in cardiovascular implants.

Keywords: Iron-based materials, Fe alloys, porosity, structure, morphology, biodegradable metals, inflammation, macrophages, endothelial cells.

***Address for correspondence**: A. Radtke, Faculty of Chemistry, Nicolaus Copernicus University in Toruń, 87-100 Toruń, Poland. Email: aradtke@umk.pl.

Introduction

Biodegradable materials used in biomedical engineering, such as stents and implants, represent a new development in the treatment of cardiovascular disease. Their use aims to eliminate durable materials that, once they have served their purpose, can cause complications such as chronic inflammation or restenosis. Magnesium and its alloys are the most commonly used medical devices in cardiology today [1,2]. They were by far the most widely studied metals for these applications, but studies have shown that in some applications, the corrosion rate of selected magnesium alloys is higher than optimal [3]. Iron and its alloys are materials with great potential in this field due to their biocompatibility, mechanical properties, and ability to degrade in the body environment; however, they are characterized by a low corrosion rate, and thus slow biodegradation. According to the literature, in the case of cardiovascular stents, complete degradation should proceed after vessel remodeling, which should take approximately four months [4]. In the case of cardiac stents, a key requirement is the combination of high mechanical strength with sufficient flexibility to allow their insertion through blood vessels to the appropriate site [5]. The scaffolds we propose still do not have optimal properties for use in stents, but they can find applications in the field of cardiology that require new, innovative solutions. Cardiac implants, such as those supporting heart valves, require mechanical support for the repaired heart valves. Biodegradable implants could temporarily support valve function during tissue regeneration and then biodegrade, allowing natural heart function to be restored. In the treatment of pediatric heart defects, such as atrial septal defects (ASDs) or ventricular septal defects (VSDs), metal occluders are used; biodegradable versions of these could allow the defect to close and the implant to biodegrade after tissue regeneration. An important criterion for selecting elements for iron alloys is to consider the regeneration of operated areas and the process of angiogenesis, which is essential for repairing damaged tissues and regenerating blood vessels. Manganese (Mn) and copper (Cu) both support this process by activating enzymes and signaling pathways involved in vascular formation. Studies have shown that manganese ions can regulate growth factors such as vascular endothelial growth factor (VEGF), which stimulates the proliferation and migration of endothelial cells, which are key to new vessel formation. Manganese plays an important role in reducing oxidative stress in endothelial cells and promotes better protection of cells from damage, and supports regenerative processes [6]. Furthermore, manganese can influence the stabilization of the hypoxia-inducible factor (HIF)-1α pathway, which is crucial in the induction of angiogenesis under hypoxic conditions, making it particularly important in repair processes after vascular surgery. In addition, manganese ions promote macrophage recruitment towards the M2 phenotype, which promotes tissue regeneration and prompts a balance in the inflammatory response, which is essential for effective wound healing [7]. Copper-containing biomaterials show potential in reducing thrombosis by modulating vascular smooth muscle cell activity and improving endothelial function, contributing to their better biological adaptation. In addition to reducing thrombosis and promoting endothelial regeneration, copper has shown the ability to increase collagen synthesis, which promotes structural strengthening of blood vessels and tissue regeneration [8]. Copper ions also modulate the immune response by stimulating macrophage differentiation towards the M2 phenotype, which promotes repair processes and reduces inflammation in surrounding tissues [8]. In addition, copper can act as a cofactor for many enzymes involved in antioxidant processes, which minimizes oxidative stress and protects cells from damage during regeneration [6,9].

The primary criterion for biodegradable implants is corrosion time. Pure iron has a relatively low corrosion rate in the physiological environment, which can be a limitation for materials that require faster biodegradation. Studies indicate that the time for full degradation of pure iron in the body can range from a few months to several years, which depends on the physiological conditions and the geometry of the implant [10]. The introduction of manganese as an alloying element into iron allows an increase in the corrosion rate through changes in the microstructure and electrochemical potentials of the material [11]. Manganese, due to its chemical properties, decreases the potential of iron, which accelerates its degradation in the physiological environment. For example, ferrite (Fe)-Mn alloys such as Fe21Mn can present significantly higher corrosion rates compared to pure iron, making them more suitable for applications requiring biodegradation throughout 6 to 24 months [10].

The novelty of this work, which we would like to articulate, is the optimization of the porosity and composition of iron-based scaffolds, leading to the production of three-dimensional systems with a defined corrosion rate and high biointegration activity, while lacking cytotoxicity and inflammatory effects. Such systems can constitute a foundation for prototype medical devices for cardiology purposes.

Materials and Methods

Samples

The materials investigated in this study were pure iron scaffolds Fe and scaffolds with addition of manganese (35 % w/w) and copper (1 % w/w): Fe, FeMn, FeCu and FeMnCu, respectively. The samples were produced using raw elemental powders: Fe (particle size $<$10 μm, 99 % purity, Batch No.: Q06H065; Alfa Aesar, Kandel, Germany), Mn (particle size $<$10 μm, 99.6 % purity, Batch No.: S2H037; Thermo Fisher Scientific, Kandel, Germany) and Cu (particle size 10 μm, 99.9 % purity, Batch No.: M14H017; Thermo Fisher Scientific, Kandel, Germany) and two types of polymer foams. A polyurethane (PU PPI15 Rekuperator, Wejherowo, Poland) with large pores and a melamine

(Mel) sponge (10 × 6.2 × 2.8 cm, Polor Sp. z o.o, Szczecin, Poland) with significantly smaller pores were used as a polymer template. The layout prepared on the template made of polyurethane foam is referred to in this manuscript as PU, while the layout produced based on melamine foam is called Mel. The powders were placed in a 50 mL centrifuge tube in the proportions given above and mixed by vibration to homogenize the powder mixture.

Preparation of the Iron Scaffolds

The polymeric sponges were suitably moulded and then soaked in a solution of 5 % polyvinyl alcohol (weight-average molecular weight (Mw) 89,000–98,000, 99+ % hydrolyzed, Batch No.: W14G024; Sigma Aldrich, Darmstadt, Germany) previously mixed with the prepared metal powders (mass ratio 1:2). The foams were then dried in a laboratory dryer for 35 minutes at 95 °C, placed in a tube furnace (Batch No.: PRW-S 70X616/110M (KW009/2018); Czylok, Jastrzębie-Zdrój, Poland) and sintered; both technological processes were adapted to the properties of the polymer used as a template as described in [12]. After synthesis, all samples were sterilized in an autoclave.

Characterization

The morphology of the produced scaffolds was studied using a Quanta scanning electron microscope with field emission (SEM, Batch No.: D9678; Quanta 3D FEG, Houston, TX, USA). Elemental analysis was illustrated using energy-dispersive X-ray spectroscopy (EDS, Batch No.: 1430-04-73; Quantax 200 XFlash 4010, Bruker AXS, Karlsruhe, Germany). Phase analysis was carried out using X-ray diffraction (XRD, Batch No.: DY1553; Philips X'Pert with X'Celerator Scientific detector; PANalytical B.V., Almelo, The Netherlands) with CuKα radiation and an incident angle of 2°.

Potentiodynamic Polarization Tests

Electrochemical degradation was studied via potentiodynamic polarization (PDP) using a potentiostat (BioLogic SP-200, Seyssinet-Pariset, France). The tests were carried out in 300 mL of Hanks' balanced salt solution (HBSS) electrolytes (Batch No.: RNBL 1223; Sigma Aldrich, St. Louis, MO, USA), open to air. Tests were carried out at 37 ± 2 °C from −250 mV to +250 mV vs. open circuit potential (OCP), after the system was allowed to stabilize considerably for 120 minutes. The scanning rate was set to 0.5 mV/s to prevent significant shifting of the OCP due to a slower scanning rate. The study was carried out in a standard three-electrode system consisting of a working electrode, a counter-electrode (platinum wire), and a reference electrode (silver/silver chloride electrode). Corrosion current densities were calculated using Tafel extrapolation.

Cell Culture

The *in vitro* studies were conducted using four cell lines: human aortic smooth muscle cells (HASMC; Cat #C-007-5C), human umbilical vein endothelial cells (HUVEC; Cat #C-015-10C), murine fibroblasts (L929; Cat #85011425), and murine macrophages (RAW 264.7; Cat #91062702). HASMC and HUVEC cells, along with their culture media components, were purchased from Thermo Fisher Scientific (Waltham, MA, USA), while L929 fibroblasts and RAW 264.7 macrophages were sourced from the European Collection of Authenticated Cell Cultures (Salisbury, UK).

HASMC cells were cultured in Medium 231 supplemented with Smooth Muscle Growth Supplement (SMGS). HUVEC cells were maintained in Medium 200 supplemented with Low Serum Growth Supplement (LSGS). To promote cell attachment and growth, culture flasks were pre-coated with Attachment Factor Protein (a gelatin-containing solution from Thermo Fisher Scientific; Cat #S-006-100), which is specifically recommended for HUVEC culture. This coating was also applied to culture plates before cell seeding for assays. L929 fibroblasts were cultured in Roswell Park Memorial Institute (RPMI) 1640 medium (Cat #R8758) supplemented with 10 % heat-inactivated fetal bovine serum (FBS; Cat #F9665), whereas RAW 264.7 macrophages were maintained in Dulbecco's Modified Eagle's Medium (DMEM, 4.5 g/L glucose; Cat # D6429) supplemented with 10 % FBS. Throughout the culture process, antibiotics (100 μg/mL streptomycin and 100 IU/mL penicillin; Cat #P4333) were added to each culture medium to maintain sterility. All cell culture reagents were obtained from Merck KGaA (Darmstadt, Germany).

All cell lines were incubated at 37 °C in a humidified atmosphere with 5 % CO_2. Cells were passaged using a 0.25 % trypsin-ethylenediaminetetraacetic acid (EDTA) solution (Merck KGaA; Cat #T4049; Darmstadt, Germany) or cell scrapers (RAW 264.7 cells) upon reaching 70–80 % confluence. All cell lines used in the experiments were maintained between passages 5 and 10. To confirm the quality of the cell cultures, we performed mycoplasma contamination testing using the Mycoplasma polymerase chain reaction (PCR) Detection Kit (GE Healthcare, Frankenburg am Hausruck, Oberösterreich, Austria; Cat #Q050-020) which confirmed the absence of contamination. The authenticity of the human cell lines (HUVEC and HASMC cells) was confirmed by short tandem repeat (STR) profiling (Malopolska Centre of Biotechnology, Jagiellonian University, Cracow, Poland), while the murine cell lines (L929 and RAW 264.7 cells) were verified based on their morphology and time-dependent growth characteristics (**Supplementary Figs. 1,2,3** and **Supplementary Table 1**).

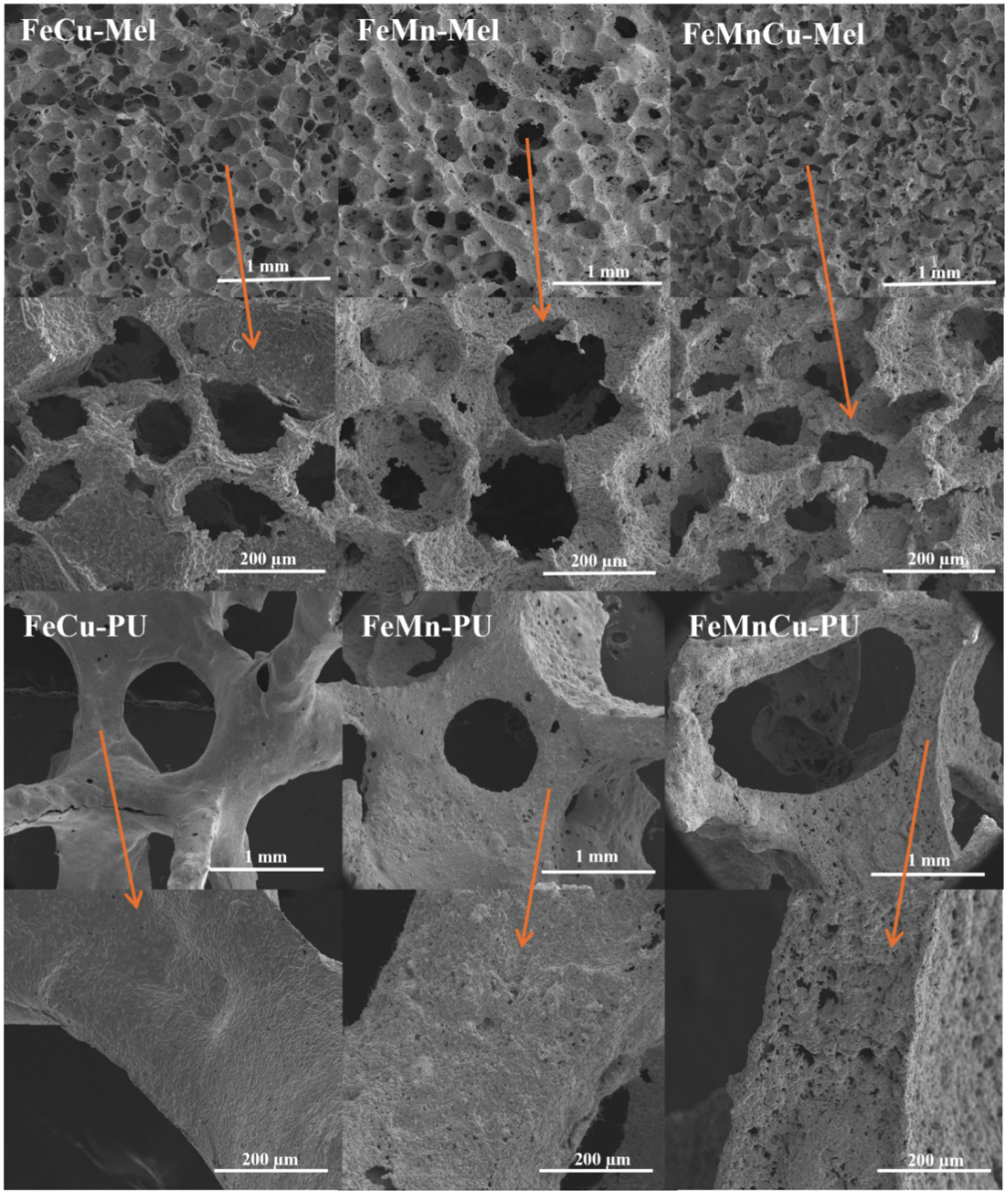

Fig. 1. SEM images showing the surface morphology of porous FeCu, FeMn and FeMnCu alloy samples obtained using melamine and polyurethane templates. Scale bar: 1 mm and 200 μm. SEM, scanning electron microscope; Fe, ferrite; Cu, copper; Mel, melamine; Mn, manganese; PU, polyurethane.

Preparation of Samples for In Vitro Studies

Prior to experimentation, the scaffolds were sterilized by autoclaving. The indirect cytotoxicity of the tested samples was assessed using the extraction method, which evaluates the potential cytotoxic effects of leachable components. This procedure was adapted from the International Organization for Standardization (ISO) guidelines, specifically ISO 10993-5:2009 [13] and ISO 10993-12:2021 [14]. The samples were placed in Petri dishes at a scaffold-to-extraction vehicle ratio of 0.2 g/mL. Extraction was carried out by incubating the samples in culture media supplemented with 10 % FBS at 37 °C with 5 % CO_2 for 72 hours. The media used for extraction corresponded to the specific cell lines: Medium 231 for HASMC cells, Medium 200 for HUVEC cells, RPMI 1640 for L929 fibroblasts, and DMEM for RAW 264.7 macrophages. Culture media with-

out samples were incubated under the same conditions and served as non-cytotoxic controls.

After incubation, the supernatants were collected, centrifuged at 2000 × g for 10 minutes, and sterilized using a 0.22 μm filter. The resulting extraction media were stored at 4 °C for no longer than 48 hours before use in cell stimulation experiments. Thus, the prepared media were used for assessing cell viability and evaluating cytokine/chemokine production by the HUVEC cells and RAW 264.7 macrophages.

Cell Viability Assessment via MTT Assay

To evaluate the potential cytotoxicity of the tested scaffolds, HASMC, HUVEC, L929 fibroblasts, and RAW 264.7 macrophages were seeded into 96-well plates at densities of 3×10^3, 5×10^3, 5×10^3, and 1×10^4 cells per well, respectively. The cells were then incubated at 37 °C in a humidified atmosphere with 5 % CO_2 for 24 hours to allow for proper attachment and acclimatization. For cell stimulation, the scaffold-derived extracts were diluted in the appropriate culture medium at four dilution ratios: 1:10, 1:6, 1:3, and 1:1 (100 % extraction medium). The cells were then exposed to these extracts for 24, and 48 hours, except for RAW 264.7 macrophages, which were treated for 24 hours only. Control cells were cultured in the corresponding dilutions of control media, which underwent the same preparation process as the extracts.

Cell viability was assessed using the 3-(4,5-dimethylthiazol-2-yl)-2,5-diphenyltetrazolium bromide (MTT; Merck KGaA, Darmstadt, Germany; Cat #M5655) assay. Following cell stimulation, the extracts were removed, and the cells were washed once with phosphate-buffered saline (PBS; Merck KGaA; Cat #P4474). Subsequently, 100 μL of MTT solution (0.5 mg/mL) prepared in phenol red-free culture medium was added to each well. The cells were then incubated at 37 °C for 3 hours. After incubation, formazan crystals were solubilized by adding 100 μL of dimethyl sulfoxide (DMSO; Merck KGaA; Cat #472301) per well, followed by horizontal mixing for 10 minutes using a microplate shaker. Optical density (OD) was measured at 570 nm (with a reference wavelength of 630 nm) using a Synergy HT Multi-Mode Microplate Reader (serial no: 264040, BioTek Instruments, Winooski, VT, USA). Results were expressed as a percentage relative to the control cells, which were cultured in the corresponding dilution of control media and set as 100 % viability. Blank wells contained extracts or control media at the respective dilutions, but without cells.

Assessment of Pro-Inflammatory Cytokine and Chemokine Production by ELISA assays

RAW 264.7 macrophages and HUVEC cells were seeded in triplicate into 24-well tissue culture plates at densities of 0.5×10^6 and 2.5×10^5 cells per well, respectively. The cells were pre-incubated for 24 hours before being stimulated with extraction media for an additional 24 hours. For treatment, the highest extraction media dilution (1:6) was selected, as it did not reduce HUVEC and RAW 264.7 cell viability below 70 % after 24 hours of stimulation, which is the ISO-defined threshold for cytotoxicity. Control cells were cultured in appropriately diluted control media.

In separate experiments, the effect of the tested specimens on pro-inflammatory cytokine/chemokine production was evaluated in a pro-inflammatory microenvironment induced by adding 100 ng/mL of lipopolysaccharide (LPS) (*Escherichia coli* O111:B4; Merck KGaA; Cat #L4391) to the culture medium. The cells were stimulated simultaneously with extraction media (dilution ratio: 1:6) and LPS for 24 hours. Control cells were stimulated with LPS and cultured in appropriately diluted control media. After treatment, culture plates were centrifuged at 800 × g for 5 minutes, and the supernatants were collected and stored at –80 °C for further analysis. To normalize cytokine/chemokine concentrations to cell number, the remaining adherent cells were stained with crystal violet (Merck KGaA; Cat #C0775). Following supernatant collection, cells were washed once with PBS, then 300 μL of 0.5 % crystal violet in 20 % methanol was added to each well and incubated at room temperature for 10 minutes. The plates were then centrifuged at 500 × g for 5 minutes, washed with water, and left to dry. After drying, 500 μL of 100 % methanol was added to each well to extract the bound crystal violet. Absorbance was measured at 595 nm, with the highest absorbance reading set as 1, and this value was used to calculate normalization coefficients for the remaining samples.

The concentrations of murine and human interleukin-6 (IL-6; Cat #M6000B and D6050B), tumor necrosis factor α (TNF-α; Cat #MTA00B and DTA00D), and monocyte chemoattractant protein-1 (MCP-1; Cat #MJE00B and DCP00) in the culture media were determined using standard ELISA kits (R&D Systems, Minneapolis, MN, USA) according to the manufacturer's instructions. Colorimetric changes were detected using a Synergy HT Multi-Mode Microplate Reader (BioTek Instruments). The total amounts of pro-inflammatory factors were normalized to the cell number, as estimated by crystal violet staining.

Statistical Analysis

All values are expressed as means ± standard deviation of the mean. Statistical analysis was conducted using a nonparametric one-way ANOVA with Tukey's post hoc test, with significance set at $p < 0.05$. The normality of the data was assessed using the Shapiro-Wilk test. Data analysis was performed using GraphPad Prism 7.0 (GraphPad Software Inc, La Jolla, CA, USA).

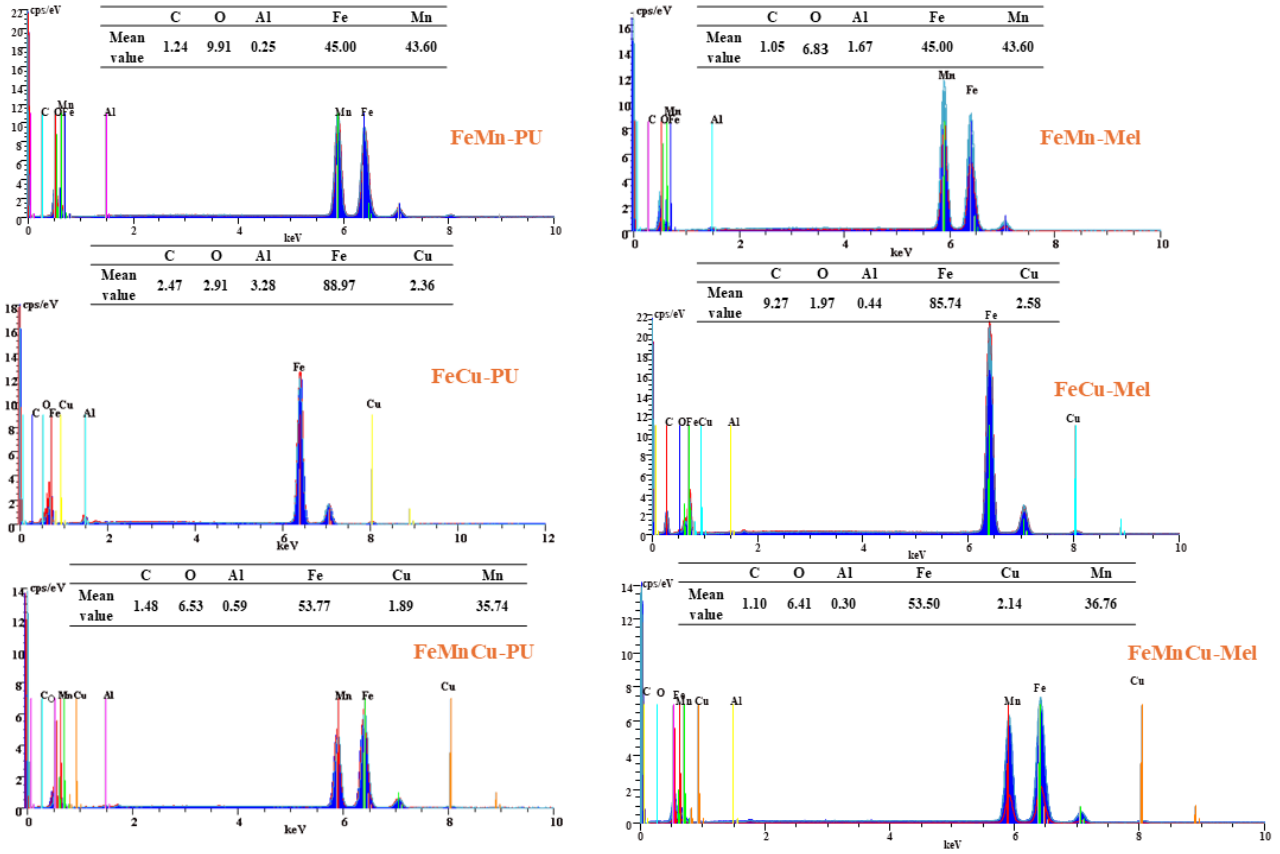

Fig. 2. EDS spectra for the analysed alloy samples: FeMn-PU, FeMn-Mel, FeMnCu-PU and FeCu-Mel, showing the detailed elemental composition of the surfaces of the samples along with the quantitative percentage of each element (Mn, Fe, Cu, O, Al).
EDS, energy-dispersive X-ray spectroscopy; C, carbon; O, oxide; Al, aluminium.

Table 1. The corrosion potential (E_{corr}) and corrosion current density (I_{corr}) values for biodegradable iron-based scaffolds with manganese and copper, fabricated using melamine and polyurethane templates.

Type of sample	E_{corr} (mV)	I_{corr} (μA)
FeMn-Mel	–475.5	11.5
FeMnCu-Mel	–443.5	8.67
FeCu-Mel	–369.4	8.11
FeMn-PU	–576.6	9.44
FeMnCu-PU	–526.8	7.56
FeCu-PU	–479.2	19.61

Fe, ferrite; Cu, copper; Mel, melamine; Mn, manganese; PU, polyurethane.

Results

Morphology and Composition Analysis

Analysis of the SEM images (Fig. 1), which show the microarchitecture of the FeCu, FeMn, and FeMnCu scaffolds made from the polyurethane and melamine templates, highlights the differences due to the presence of the different alloying elements. The microarchitecture of FeCu-doped scaffolds exhibits distinct differences depending on the type of template employed. Samples produced using the melamine template present a pore size of 0.1–0.35 mm. The average pore size of scaffolds produced using the polyurethane template is 0.7–1.6 mm. Materials made using a melamine sponge template have a porosity of approximately 21 %, while the template used to manufacture the scaffolds has a large number of small pores, but a significant number of pores are melted during the thermal process. The use of polyurethane foam, which has a large diameter and number of pores, results in a significantly higher porosity of 97 %. The FeCu-Mel foam is characterized by a porous structure with varying pore sizes, with the presence of both large, irregular pores and smaller pores in the walls of larger cells. The pore walls in FeCu-Mel are relatively smooth, but corrugated and irregular in areas, and appear dense and compact on a microstructural scale. In contrast, the FeCu-PU scaffold, on a polyurethane template, presents a more regular pore morphology, larger and homogeneous, with a near-circular shape. The FeCu-PU pore walls are noticeably smoother and thinner than in FeCu-Mel, and their microstructure is smoother and more open-worked, with visible connections between the pores. In the FeMn-doped scaffold series, the influence of template type was also noticed. The FeMn-Mel foam, like FeCu-Mel, shows a porous architecture, which is less regular than in the

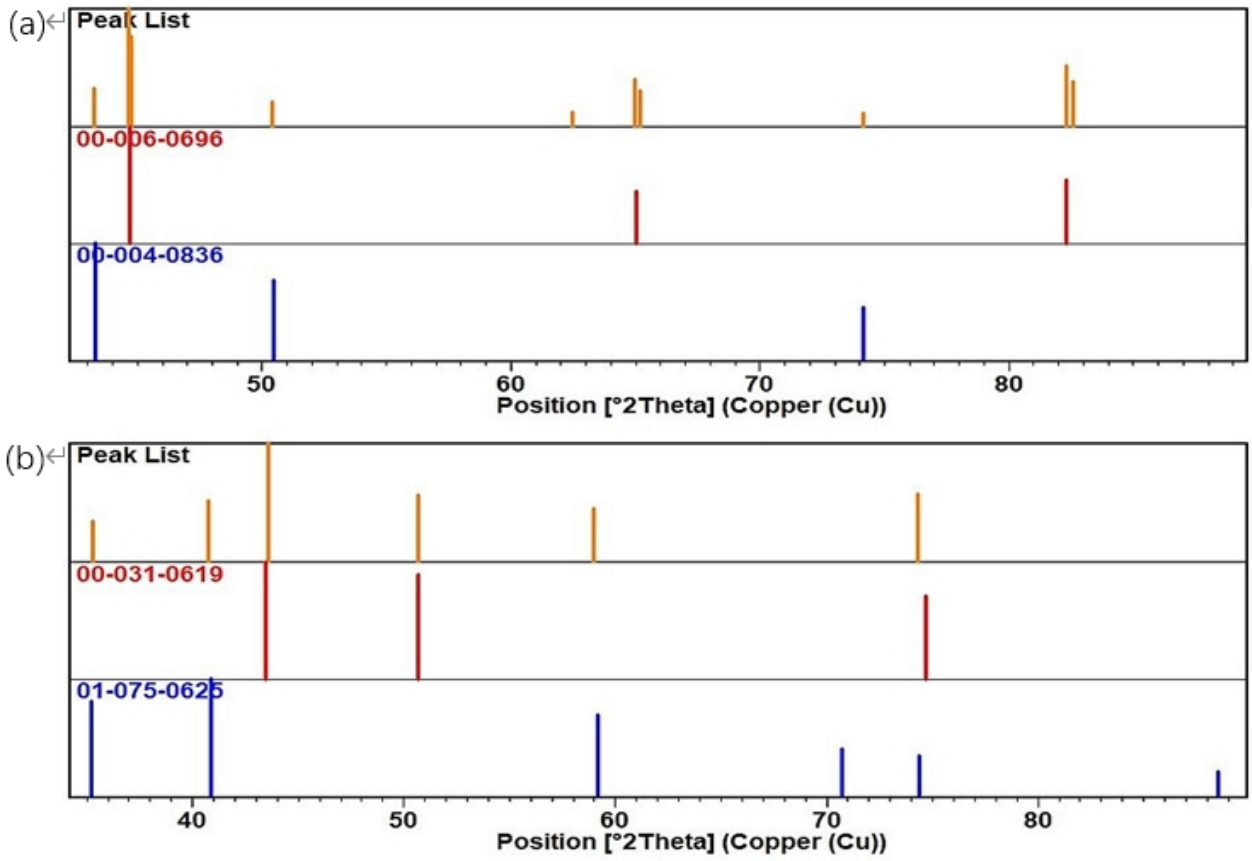

Fig. 3. X-ray diffractograms of the analyzed samples. (**a**) Registered diffraction peaks of the FeMn sample with the ICDD database reference peaks for austenite (Fe, C) and manganese oxide (MnO). (**b**) Registered diffraction peaks of the FeMn sample with the ICDD database reference peaks for ferrite (Fe α) and copper (Cu). ICDD, International Center for Diffraction Data.

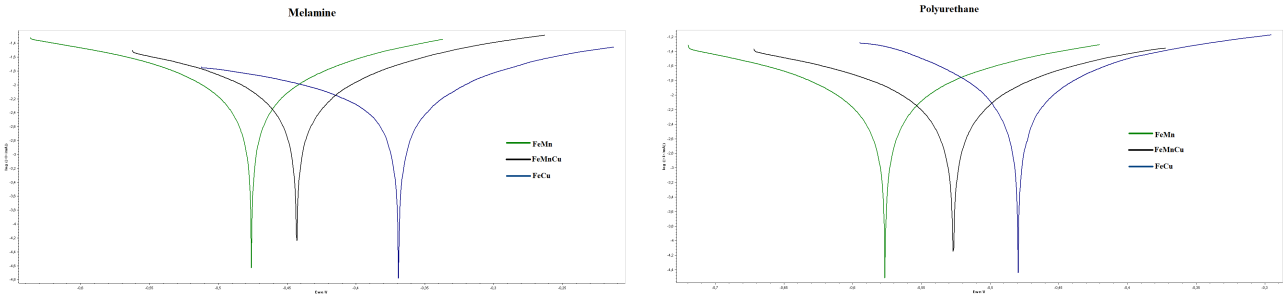

Fig. 4. Potentiodynamic polarization curves for the investigated iron-based scaffolds: FeMn-Mel, FeMn-PU, FeMnCu-Mel, FeMnCu-PU, FeCu-Mel and FeCu-PU, showing the electrochemical characteristics and corrosion degradation tendencies in HBSS solution. The curves illustrate the influence of scaffold type (Mel/PU) and alloy composition (FeMn, FeMnCu, FeCu) on the corrosion current density and corrosion potential, indicating the varying degradation rates under *in vitro* conditions. HBSS, Hanks' balanced salt solution.

FeCu series, with a higher proportion of irregular pores and varying pore sizes. It is characterised by thicker, rough, and porous walls, with more defects and irregularities compared to FeCu-Mel. FeMn-PU foam, analogous to FeCu-PU, is characterised by a more regular pore structure, larger, uniformly shaped pores, and thinner and smoother walls than FeMn-Mel. The FeMn-PU wall architecture is compact, but less dense than in FeCu-PU, with interconnectivity between pores. Double-doped FeMnCu foams show a pore structure with intermediate features. FeMnCu-Mel foam has a pore structure less regular than in the PU series, but more regular than FeMn-Mel. The pore size is varied, with a lower degree of variation than in FeMn-Mel. The pore walls of FeMnCu-Mel are thicker than in the PU series, smoother than in FeMn-Mel, and the microstructure is compact, although with some irregularities. The FeMnCu-PU foam

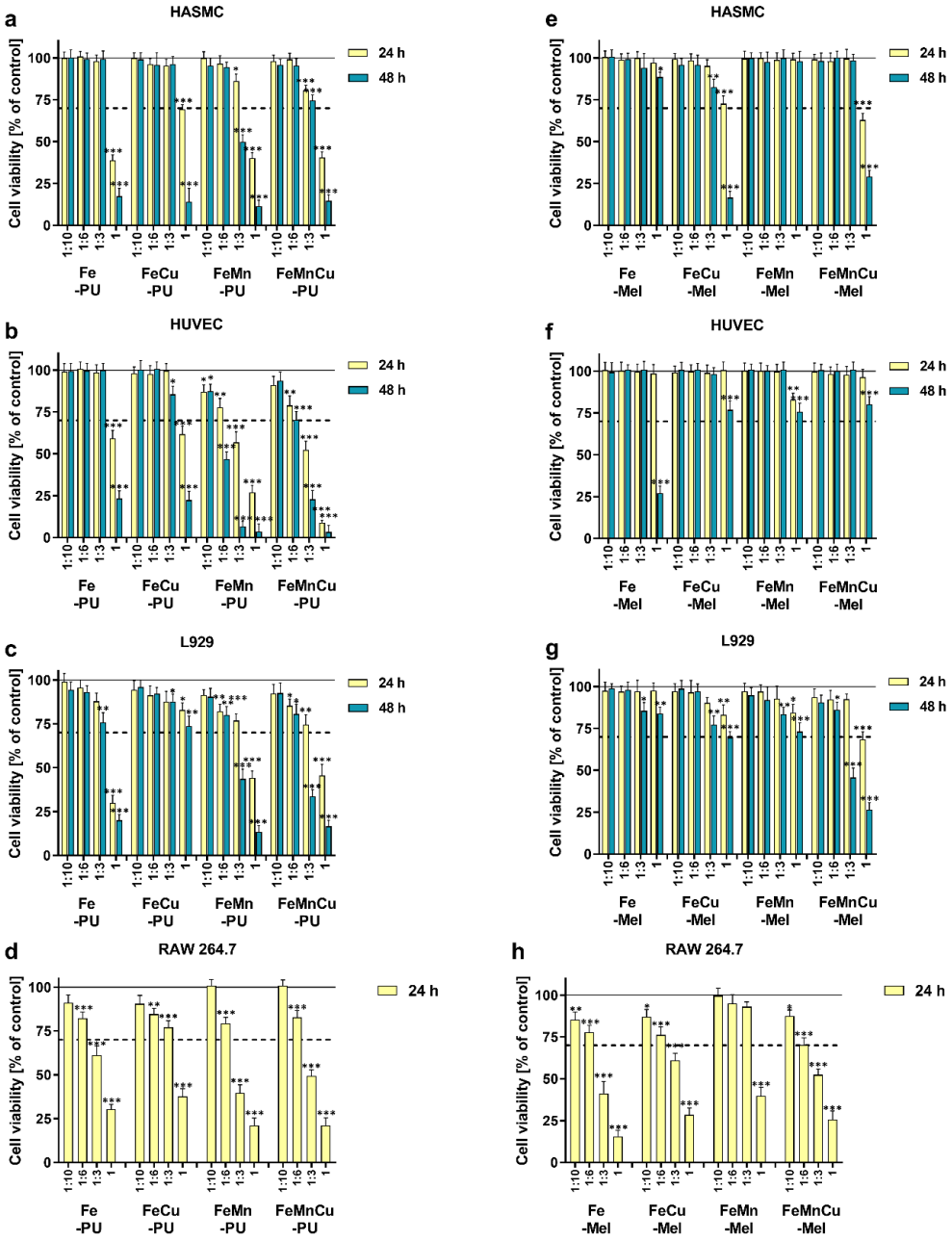

Fig. 5. Viability of cells stimulated with extraction media from the tested scaffolds. Human aortic smooth muscle cells (HASMC; **a,e**), human umbilical vein endothelial cells (HUVEC; **b,f**), murine fibroblast cell line L929 (**c,g**) and murine RAW 264.7 macrophages (**d,h**) were stimulated with extracts derived from the tested scaffolds. Cells were stimulated for 24 and 48 hours (only 24 hours in the case of RAW 264.9 cells) with extracts diluted in an appropriate culture medium at four dilution factors: 1:10, 1:6, 1:3, and 1. Cell viability, assessed using the MTT assay, was expressed as a percentage (± S.D.) relative to control cells cultured in corresponding control media. Asterisks indicate statistically significant differences between control cells (set at 100 %; solid line) and extract-treated cells (*$p < 0.05$; **$p < 0.01$; ***$p < 0.001$). According to ISO standards, the dashed line represents potential cytotoxicity, defined by a cell viability drop below 70 %. ISO, International Organization for Standardization.

stands out as having the most regular pore structure of all the samples, with large, homogeneous pores of regular circular shape and the thinnest and smoothest walls. The microstructure of the FeMnCu-PU walls is smooth and perforated, with clear connections between the pores.

The elemental composition was confirmed using EDS spectroscopy (Fig. 2). The manganese content of 35 wt % was used to prepare the systems. EDS analysis of both FeMn-PU and FeMn-Mel samples showed that the amount of manganese in the samples is much higher than

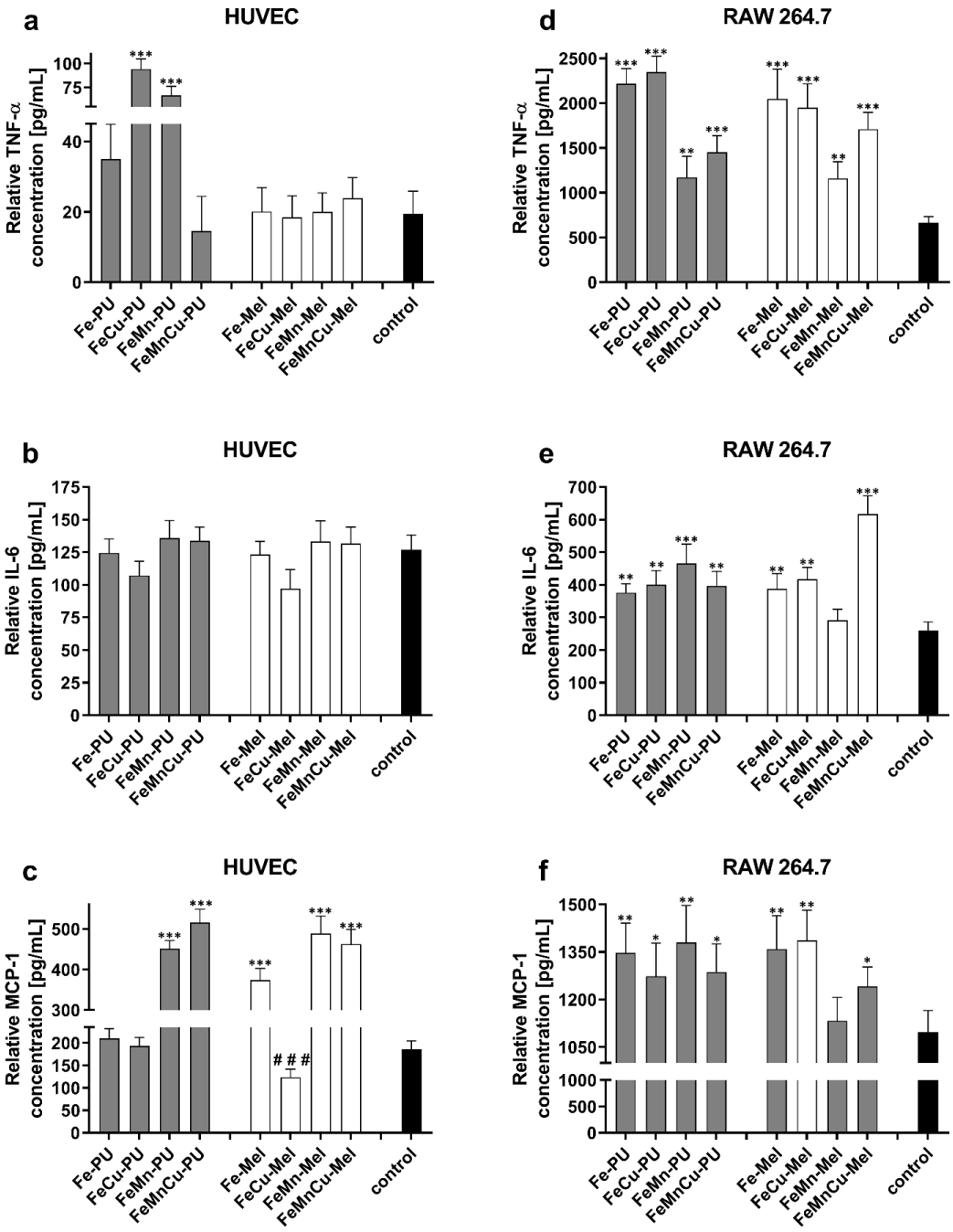

Fig. 6. Production of pro-inflammatory cytokines by cells stimulated with extraction media from the tested scaffolds. Human umbilical vein endothelial cells (HUVEC; **a–c**) and RAW 264.7 macrophages (**d–f**) were stimulated with extraction media at a 1:6 dilution for 24 hours. The concentrations of tumor necrosis factor-α (TNF-α), interleukin-6 (IL-6), and monocyte chemoattractant protein-1 (MCP-1) in the culture media were assessed using ELISA assays. Cytokine levels were normalized to the total number of viable cells, as determined by crystal violet staining. Data represent the mean ± S.D. from three independent experiments. Asterisks indicate significant increases in cytokine levels compared to control (non-treated) cells (*$p < 0.05$; **$p < 0.01$; ***$p < 0.001$), while hashes denote significant decreases relative to the control (###$p < 0.001$).

expected. EDS analysis revealed significant differences in the elemental composition of the metal scaffolds, which were directly related to the type of polymer template used, polyurethane and melamine ones. The microstructural dissimilarities of the two foams, i.e., pore size and surface area in contact with the metal powders, had a key impact

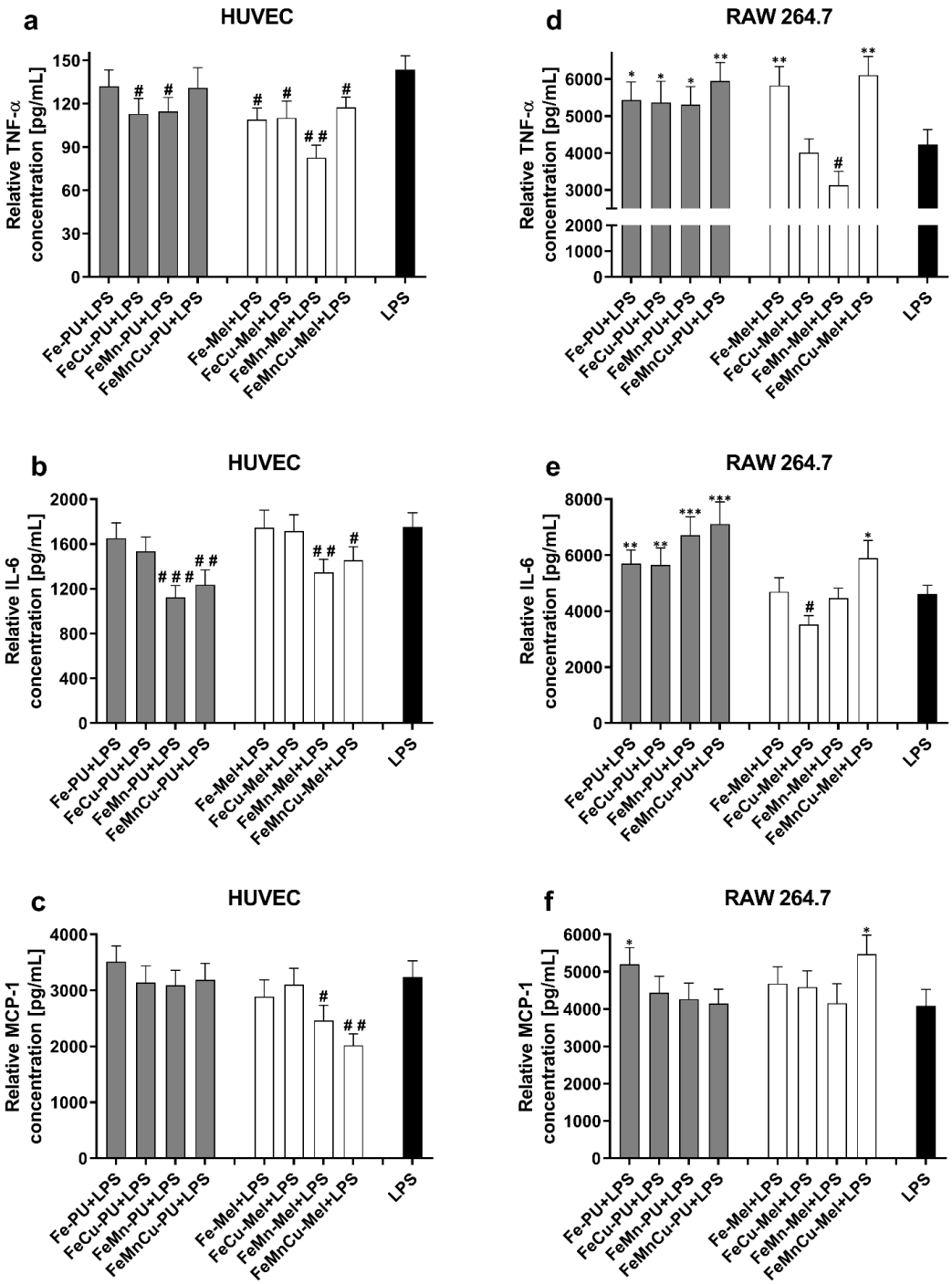

Fig. 7. Production of pro-inflammatory cytokines by cells co-stimulated with extraction media from the tested scaffolds and lipopolysaccharide (LPS). Human umbilical vein endothelial cells (HUVEC; **a–c**) and RAW 264.7 macrophages (**d–f**) were simultaneously stimulated with extraction media (1:6 dilution) and LPS (100 ng/mL) for 24 hours. The concentrations of tumor necrosis factor-α (TNF-α), interleukin-6 (IL-6), and monocyte chemoattractant protein-1 (MCP-1) in the culture media were quantified using ELISA assays. Cytokine levels were normalized to the total number of viable cells, as determined by crystal violet staining. Data are presented as the mean ± S.D. from three independent experiments. Asterisks indicate significant increases in cytokine levels compared to positive control cells stimulated with LPS alone (*$p < 0.05$; **$p < 0.01$; ***$p < 0.001$), while hashes denote significant decreases relative to the LPS-treated control (#$p < 0.05$; ##$p < 0.01$; ###$p < 0.001$).

on elemental dispersion, phase boundary interactions, and polymer removal efficiency during sintering. In scaffolds prepared on the PU template, characterized by larger pores, there is a tendency to form larger clusters of metallic phases, leading to local fluctuations in elemental composition. EDS spectra for Mel-based scaffolds characterize an increased proportion of carbon (C) and oxygen.

Material Phase Characteristics

Phase analysis of the samples was carried out by X-ray diffraction (XRD). As a result, diffractograms were recorded for FeMn and FeCu alloys, the analysis of which allowed the identification of crystalline phases. In **Supplementary Materials** there are two XRD spectra of FeCu and FeMn samples (**Supplementary Figs. 4,5**). The experimental data were compared with reference standards contained in International Center for Diffraction Data (ICDD) databases. Diffractograms of the performed samples and standards are shown in Fig. 3. The diffractogram of Fig. 3**a** identified the dominant presence of an austenitic (Fe, C) phase, characterized by a regular lattice system of the fcc type, with a space group of Fm-3m and a crystal lattice parameter of a = 3.6000 Å. The characteristic diffraction reflection for austenite was observed at an angle of 2θ of approximately 43.47°, which corresponds to the crystal plane (111). The intensity and position of this peak clearly indicate the presence of this phase in the analyzed material. In addition, the presence of reflections at 2θ angles 50.67° and 74.68°, corresponding to crystal planes (200) and (220), further confirms the presence of an austenitic phase. The second major crystalline phase identified in the sample is manganese oxide (MnO), characterized by a regular fcc-type lattice system with space group Fm-3m and crystal lattice parameter a = 4.4150 Å. Reflections characteristic of this phase were observed around 2θ angles equal to about 35.18° (plane (111)) and 40.85° (plane (200)). The intensity of these peaks allows us to confirm the presence of MnO as an additional phase in the sample. Analysis of the FeCu diffractogram (Fig. 3**b**) showed the predominant presence of a ferritic phase (α-iron), characterized by a regular spatially centered arrangement (bcc) with space group Im-3m and crystal lattice parameter a = 2.8664 Å. The characteristic diffraction reflection for ferrite was observed at 2θ angle 44.67°, which corresponds to the crystal plane (110). In addition, the presence of reflections at 2θ angles of about 65.02° and 82.34°, corresponding to crystal planes (200) and (211), confirms the presence of a ferritic phase. In addition, the presence of a copper (Cu) phase, characterized by an fcc-type regular structure with space group Fm-3m and crystal lattice parameter a = 3.6150 Å, was observed in the sample. Diffraction reflections characteristic of Cu were identified at 2θ angles of 43.30°, 50.43° and 74.13°, corresponding to the (111), (200) and (220) planes. The intensity of these reflections confirms the presence of copper as an additional phase.

Degradation Test

Potentiodynamic polarization (PDP) tests were a key step in assessing the degradation rate of scaffolds fabricated using melamine and polyurethane templates made from different alloys—FeMn, FeMnCu and FeCu—in an environment mimicking physiological fluids. This research was designed to provide preliminary data on the potential biodegradation rate of these materials, which are being considered for use in biodegradable cardiac implants. The determination in potentiodynamic tests of the I_{corr} value is directly related to the corrosion rate of the investigated material. Higher I_{corr} values mean that the material degrades faster, which is significant regarding biodegradable materials. The second parameter determined is the E_{corr}, which indicates the thermodynamic susceptibility of the material to corrosion. Analysis of the polarisation curves (Fig. 4) obtained clearly indicates that the type of alloy used significantly determines the degradation of the scaffold, while the type of scaffold used has less influence.

In Table 1 there are data about corrosion potential (E_{corr}) and corrosion current density (I_{corr}) values for biodegradable iron-based scaffolds with manganese and copper, fabricated using melamine and polyurethane templates. The scaffolds consisting of FeMn consistently showed the highest values of corrosion current density among the tested materials, which correlates with a more intense corrosion process and thus suggests the fastest degradation of the material in the tested environment. In contrast, at the other extreme, the FeCu scaffolds were characterised by the lowest current densities. This in turn indicates the slowest degradation of this alloy compared to the others. The FeMnCu scaffolds, presented an intermediate behaviour, occupying positions between FeMn and FeCu in terms of degradation rate, as manifested by the average values of the corrosion current densities. The influence of the type of scaffold used, on the degradation process, is noticeable.

Evaluation of Cytotoxicity and Inflammatory Response in Cells Stimulated with Scaffold-Derived Extracts

The cytotoxicity of the tested scaffolds was assessed using four cell lines and an extraction method. This approach evaluates the impact of substances released from the implant surface upon contact with surrounding fluids, which is crucial for materials in blood-contacting implants. The evaluation of cell viability revealed a dose- and time-dependent decline in cell survival across most tested scaffolds, but mainly at higher extract concentrations. When comparing the toxic effects of scaffolds based on polyurethane and melamine, it is clear that all materials made from melamine are less toxic to HASMC, HUVEC, and L929 cells than their PU counterparts. For the Mel-based scaffolds, toxic effects on HASMC cells were observed only for undiluted extracts of FeCu-Mel and FeMnCu-Mel samples (Fig. 5**e**). In contrast, for HUVEC

cells, toxicity was evident only with the undiluted Fe-Mel extract (Fig. 5**f**). Regarding L929 fibroblasts, toxic effects were seen with both the 1:3 diluted and undiluted extracts from the FeMnCu-Mel material (Fig. 5**g**). The evaluation of cell viability for three different cell types stimulated with extracts made from PU showed that the toxic effect was mainly observed with undiluted extracts (except for the extract from the FeCu-PU sample, where no toxic effect was seen on L929 fibroblasts; Fig. 5**c**), as well as some of the 1:3 diluted extracts from the FeMn-PU and FeMnCu-PU samples (Fig. 5**a–c**). In the case of RAW 264.7 macrophages, a toxic effect was observed for the undiluted extracts from all the tested samples, as well as for the 1:3 diluted extracts, except for FeMn-PU and FeMn-Mel samples, which showed no toxic effect (Fig. 5**d,h**).

In the next experiments, we investigated the effects of the tested extracts on the secretion of key inflammatory mediators (IL-6, TNF-α, and MCP-1) by HUVEC endothelial cells and RAW 264.7 macrophages. The results showed that, in the case of HUVEC cells, extracts made from Mel did not induce increased production of TNF-α (Fig. 6**a**) or IL-6 (Fig. 6**b**) compared to control cells. However, an elevated secretion of MCP-1 was noticed, except for the FeCu-Mel extract, where the level of this chemokine was lower than in control cells ($p < 0.001$; Fig. 6**c**). On the other hand, extracts from PU-based scaffolds did not induce increased production of IL-6 (Fig. 6**b**), but some extracts led to elevated secretion of TNF-α (FeCu-PU and FeMn-PU samples; Fig. 6**a**) and MCP-1 (FeMn-PU and FeMnCu-PU samples; Fig. 6**c**). The extracts' impact on the secretion of pro-inflammatory factors by RAW 264.7 macrophages revealed that the studied scaffolds significantly influence the cells' ability to release these factors. Elevated production of IL-6, TNF-α, and MCP-1 was observed in comparison to control cells for all the tested samples (Fig. 6**d–f**), except for the FeMn-Mel extract, which did not induce increased secretion of MCP-1 (Fig. 6**f**).

In subsequent stages of the study, the potential anti-inflammatory properties of the scaffolds were evaluated by co-stimulating cells with LPS and material extracts. The inflammatory response, based on IL-6, TNF-α, and MCP-1 levels, was compared to LPS-only controls. As shown in Fig. 7, in a pro-inflammatory environment, extracts from the FeMn-Mel and FeMnCu-Mel samples inhibited the production of all the tested factors by HUVEC cells. Additionally, it was observed that the secretion of IL-6 by these cells is reduced by extracts from the FeMn-PU and FeMnCu-PU samples (Fig. 7**b**). Regarding TNF-α levels, all tested extracts, except for those from the Fe-PU and FeMnCu-PU samples, showed also inhibitory effects on the secretion of this cytokine (Fig. 7**a**). Moreover, co-stimulation of RAW 264.7 macrophages revealed that the inhibitory effect on the secretion of TNF-α and IL-6 occurred due to the presence of extracts from the FeMn-Mel and FeCu-Mel samples in the pro-inflammatory environment (Fig. 7**d,e**, respectively). On the other hand, all PU-based samples induced increased production of TNF-α and IL-6 compared to cells stimulated with LPS alone. In the case of MCP-1 level secreted by macrophages, it was observed that the Fe-PU and FeMnCu-Mel samples slightly enhanced the secretion of this chemokine in the presence of LPS. At the same time, all other extracts did not induce significant changes in their level (Fig. 7**f**).

Discussion

Template-based processes with the use of metallic powders (Fe, Mn, Cu) and polymeric templates gave different 3D-scaffolds, differing in composition, structure, and morphology. When analyzing scanning electron microscopy images, it can be seen that the addition of manganese in both templates (FeMn-PU, FeMn-Mel) results in a significant increase in the roughness of the scaffold surface. The pore walls become less smooth, and minor microstructures appear on their surface. Increased irregularity of pore shape is also apparent; instead of uniform and well-demarcated edges, more ragged structures appear. The addition of manganese to iron increases the porosity of the system [15,16]. The combination of manganese and copper in both templates (FeMnCu-PU, FeMnCu-Mel) increases the morphological complexity of the rock further. The pores become even more irregular, and the pore walls show numerous microstructural depressions and textural variations. Compared to FeMn-PU, FeMnCu-PU is characterised by a more developed microstructure, with the presence of smaller substructures within the walls. In addition, the surface of the scaffold is more porous and the texture less uniform. The important point is that the porosity of the material increases the surface area available for degradation, which accelerates degradation. Implants with macropores (150–300 μm) and interconnected pores have a larger surface area for corrosion, which affects the rate of corrosion product formation [17]. Referring to the fact stated in the Results chapter that EDS analysis of both FeMn-PU and FeMn-Mel samples showed that the amount of manganese in the sample is much higher than expected, it can be explained by the fact that during the powder metallurgy process, the distribution of elements may not be completely homogeneous. In particular, manganese and copper may not show a uniform distribution in the iron matrix. This could result in areas locally enriched in manganese or copper and areas relatively poorer in these elements [18]. The cause could be the sublimation of manganese during sintering. Manganese has a high vapour pressure, which causes it to sublimate during sintering. This in turn leads to the loss of manganese from some areas and its condensation in other [19]. EDS spectra for scaffolds prepared on the PU template tend to show a lower proportion of carbon and oxygen, suggesting relatively more efficient removal of the polymer template. Additionally, the oxygen present in manganese alloys is, from a thermodynamic point of view,

almost impossible to prevent oxidation of Mn vapour even under such conditions [20]. An increased proportion of carbon and oxygen on the EDS spectra of scaffolds prepared on the Mel template may indicate difficulties in removing residual polymer from inside the dense microstructure. Furthermore, EDS analysis revealed differences in the intensity of the peaks corresponding to individual elements depending on the template. Samples obtained on the basis of the melamine template often showed stronger peaks for oxygen, which may suggest increased oxidation of metals at the metal-polymer interface, resulting from a larger contact area [12]. Considering the phase characteristics of the studied materials, it is necessary to analyze the references regarding the influence of metallic additives. Literature data reports that manganese is a stabilizing element of fcc(γ). The addition of manganese to iron leads to austenitic steel [21]. The presence of manganese (II) oxide instead of pure manganese in the analyzed samples is due to manganese's high affinity to oxygen [16]. During the sintering process, which takes place at high temperatures, the oxygen present in the pores promotes the oxidation of manganese to MnO. Moreover, these oxides show high stability at temperatures above 800 °C [22], which hinders their reduction [23]. When FeCu samples are analyzed, where copper is present in only 1 %, signals characteristic of both the bcc structure of iron and signals characteristic of the fcc structure of copper are visible. The small addition of copper to iron results in the observation of bcc (110) and (200) and fcc (111) and (220) reflections, and as the amount of copper increases, the signals corresponding to the bcc structure of iron are completely suppressed [24,25]. The analysis of the polarisation curves and data in Table 1 shows that polyurethane-based scaffolds have slightly lower E_{corr} values compared to melamine-based scaffolds, regardless of the alloy used. The more negative the E_{corr} potential, the greater the tendency to oxidise in a given environment [26]. The subtle difference suggests that melamine-based scaffolding may slightly slow down the degradation process compared to polyurethane-based scaffolding. The association is related to surface morphology; the melamine scaffold is more densely packed, while the polyurethane template has lower packing and higher overall porosity [12]. In the literature, the addition of copper to Fe-Mn alloys can increase the corrosion rate, but these effects depend on the copper content and microstructure of the alloy. Cu particles dispersed in the microstructure act as cathodic sites towards the matrix, increasing the degradation rate through a micro-galvanic corrosion mechanism [16]. Stents made of pure iron implanted in the pig aorta did not induce any local or systemic toxicity [27]. However, due to the very low degradation rate of pure iron in the physiological environment, such implants show reactions similar to those observed in solid applications [28]. To increase the degradation rate of Fe-based materials, iron is doped with manganese; the resulting alloy shows an increased degradation rate compared to pure iron [29,30]. Manganese lowers the standard electrode potential of iron, making the iron matrix more susceptible to corrosion through the formation of micro-cells [31]. On the other hand, the formation of oxide and hydroxide layers can also occur during corrosion. Manganese reacts with oxygen and water to form oxides and hydroxides, which are deposited on the surface of the material. The degradation products include metal hydroxides and calcium and phosphorus layers. These layers can affect the rate of corrosion by acting as a diffusion barrier, slowing the exchange of ions between the substrate and the solution [32]. The addition of several percent of copper indicates an increase in corrosion potential; however, the presence of free copper particles dispersed in the microstructure acts as cathodes relative to the matrix, accelerating degradation through a micro-galvanic corrosion mechanism [16].

The biocompatibility and toxicity of metallic materials, including iron-based scaffolds, are primarily governed by the type and concentration of released ions and degradation products [33]. These factors affect cellular behavior, tissue compatibility, and overall implant safety. To better reflect prolonged *in vivo* conditions, we extended the extraction duration to 72 hours, beyond the ISO 10993-12 recommendation of 24 hours. This approach captures long-term ion release expected after implantation.

In this study, the potential cytotoxicity of the scaffolds was evaluated using HASMC, HUVEC, and L929 fibroblasts. These cell types are essential for assessing cardiovascular implant biocompatibility, as stents interact first with endothelial and smooth muscle cells during wound healing, and later are mainly surrounded by smooth muscle cells [34]. HASMCs maintain vascular structure and regulate tone, ensuring implant stability [35]. HUVECs are widely used as an endothelial model, regulating smooth muscle behavior and preventing platelet activation [36,37]. The L929 fibroblast line is a standard tool for biomaterial cytotoxicity testing [38]. As fibroblasts form the peri-implant mucosal seal that prevents epithelial ingrowth, their inclusion extends biocompatibility assessment beyond vascular responses [39]. We also assessed the impact of scaffolds on the macrophage viability since these cells, alongside endothelial cells, are well-recognized as key regulators of the inflammatory response, critically involved in infection control and the host reaction to implanted biomaterials [10]. The results showed that Mel-based scaffolds demonstrated consistently lower cytotoxicity compared to PU-based materials across all tested cell types. For HASMC, HUVEC, and L929 cells, toxic effects were mainly associated with undiluted or 1:3 diluted extracts of selected Mel and PU scaffolds. Notably, RAW 264.7 macrophages were the most sensitive, exhibiting reduced viability even with some diluted extracts, particularly from PU-based samples. However, when analyzing these results, it is essential to consider that, according to ISO standards, a material is deemed toxic if it causes a reduction in cell viability below 70 %. More-

over, *in vivo*, a cardiovascular implant in contact with surrounding bodily fluids, primarily blood, is subjected to continuous interaction with these fluids. This results in the concentration of substances released from the implant's surface being consistently diluted due to the ongoing flow. Therefore, the implant is not exposed to 100 % extract concentration under natural conditions, as would be the case in a controlled *in vitro* environment [40]. The elevated cytotoxicity of PU-based scaffolds may result from their higher porosity and faster degradation, leading to more substantial iron ion release. While iron ions are vital in small amounts, excess concentrations generate reactive oxygen species (ROS) via Fenton reactions, leading to oxidative stress, lipid peroxidation, and ultimately cell death via ferroptosis and apoptosis [41,42].

It is well established that cardiovascular implants typically undergo a process of wound healing. Moreover, following the initial interaction between blood and the material, inflammatory responses are triggered around the implanted device [36]. Endothelial cells and macrophages are believed to be the key cells involved in this response by, among others, releasing cytokines (e.g., IL-6, TNF-α) and chemokines (e.g., MCP-1), which orchestrate immune cell recruitment and activation [43,44]. Our cytokine data show that Mel-based extracts, particularly FeMn-Mel and FeCu-Mel, did not stimulate IL-6 or TNF-α secretion in HUVECs. MCP-1 levels were modestly elevated, except for FeCu-Mel, where MCP-1 was reduced. In contrast, PU-based extracts, such as FeMn-PU and FeMnCu-PU were associated with significantly increased TNF-α and MCP-1 production. Macrophages displayed elevated cytokine levels (TNF-α, IL-6, MCP-1) for all tested extracts except FeMn-Mel, which did not induce MCP-1. These findings indicate that FeMn-Mel and FeCu-Mel scaffolds provoke minimal inflammatory responses under native conditions [42]. This can be attributed to their lower porosity and slower degradation rates, which result in reduced ion release and oxidative stress [33].

After assessing the effects of the scaffolds on the production of pro-inflammatory mediators, we further investigated whether these materials could modulate inflammation triggered by bacterial infection. To simulate this phenomenon, both cell types were co-stimulated with the scaffold extracts and bacterial LPS, a well-known pyrogenic factor used to induce an *in vitro* inflammatory state [45]. Our findings indicate that scaffold composition and architecture jointly shape the inflammatory response. In a pro-inflammatory environment, FeMn-Mel and FeMnCu-Mel extracts reduced IL-6, TNF-α, and MCP-1 secretion by HUVECs, whereas PU-based scaffolds, such as Fe-PU and FeMnCu-PU, enhanced cytokine release, suggesting a stronger pro-inflammatory potential. Similarly, FeMn-Mel and FeCu-Mel extracts suppressed LPS-induced TNF-α and IL-6 production in RAW 264.7 macrophages, supporting their anti-inflammatory activity. These observations are consistent with prior studies demonstrating that manganese- and copper-containing biomaterials can promote macrophage polarization toward an anti-inflammatory M2 phenotype, thereby attenuating pro-inflammatory cytokine production [46]. Moreover, mechanistically, manganese-containing materials have been shown to enhance endogenous antioxidant defenses, reducing oxidative stress and inflammation [47], while copper can modulate macrophage activity toward an anti-inflammatory phenotype and support endothelial regeneration [48].

In contrast, PU-based extracts generally promoted cytokine secretion, reinforcing the pro-inflammatory response. This observation aligns with the concept that scaffold architecture and porosity significantly influence both degradation behavior and host response. Implants with large, interconnected pores are more susceptible to inflammatory activation, likely due to accelerated corrosion and uncontrolled ion release [49]. Interestingly, the slight increase in MCP-1 observed for certain extracts (Fe-PU and FeMnCu-Mel) may indicate a differential regulation of chemokines vs. cytokines, a phenomenon previously reported for Fe-based biomaterials. This selective modulation of chemokines could influence the recruitment of immune cells and subsequent tissue remodeling. Moreover, the physical characteristics of biomaterials, including surface properties, are known to affect chemokine secretion, such as MCP-1 [50]. Overall, these comparisons highlight that scaffold architecture and alloying elements jointly determine the inflammatory outcome, with Mel-based FeMn and FeCu scaffolds showing the most consistent anti-inflammatory potential.

Among all the tested materials, the FeCu-Mel and FeMn-Mel samples demonstrated the most pronounced anti-inflammatory potential, as they consistently inhibited key pro-inflammatory cytokines in both endothelial cells and macrophages. These findings indicate that these two Mel-based scaffolds, could serve as promising candidates for modulating inflammation in tissue engineering applications, especially in inflammatory environments associated with bacterial infections.

Conclusions

In conclusion, considering the impact on the viability of key cells essential for the proper implantation of cardiovascular devices, such as endothelial cells, aortic smooth muscle cells, and fibroblasts, as well as the assessment of potential inflammatory induction, melamine-based scaffolds containing Mn or Cu demonstrate the greatest application potential. Additionally, these materials also show significant anti-inflammatory effects, further supporting their suitability for the use in cardiovascular implants.

List of Abbreviations

HASMC, human aortic smooth muscle cells; HUVEC, human umbilical vein endothelial cells; LPS, lipopolysaccharide; MCP-1, monocyte chemoattractant protein-1; Mel, melamine; PU, polyurethane; TNF-α, tumor necrosis factor α; IL-6, interleukin-6; SEM, scanning electron microscope; EDS, energy-dispersive X-ray spectroscopy; XRD, X-ray diffraction; PDP, potentiodynamic polarization; HBSS, Hanks' balanced salt solution; OCP, open circuit potential; MnO, manganese oxide; ICDD, International Center for Diffraction Data; Fe, ferrite; Cu, copper; ISO, International Organization for Standardization; HIF, hypoxia-inducible factor; FBS, fetal bovine serum; DMEM, Dulbecco's Modified Eagle's Medium; PBS, phosphate-buffered saline; O, oxide; C, carbon.

Availability of Data and Materials

The datasets used and/or analyzed are available from the corresponding author on reasonable request.

Author Contributions

GG, MG, and AR designed the research study. GG, MG, TJ, SW, PM, and AR developed methodology. GG, MG, TJ, and PM performed validation and conducted investigation. GG, MG, TJ, and SW carried out formal analysis. GG, MG, TJ, and AR did data curation. GG, MG, TJ, SW, and AR wrote the original draft. GG, MG, and TJ created visualization. AR managed supervision and project administration. All authors read and approved the final manuscript.

Ethics Approval and Consent to Participate

Not applicable.

Acknowledgments

We gratefully acknowledge the important assistance from Professor Piotr Piszczek (Faculty of Chemistry, Nicolaus Copernicus University in Toruń), during the preparation of the iron scaffolds.

Funding

The research was funded within grant Preludium BIS (No. 2019/35/O/ST5/00405) by the National Science Centre, Poland.

Conflict of Interest

The authors declare no conflict of interest.

Supplementary Material

Supplementary material associated with this article can be found, in the online version, at https://doi.org/10.22203/eCM.v054a09.

References

[1] Gąsior G, Szczepański J, Radtke A. Biodegradable Iron-Based Materials-What Was Done and What More Can Be Done? Materials. 2021; 14: 3381. https://doi.org/10.3390/ma14123381.

[2] Qi Y, Qi H, He Y, Lin W, Li P, Qin L, *et al*. Strategy of Metal-Polymer Composite Stent To Accelerate Biodegradation of Iron-Based Biomaterials. ACS Applied Materials & Interfaces. 2018; 10: 182–192. https://doi.org/10.1021/acsami.7b15206.

[3] Kumar K, Gill RS, Batra U. Challenges and opportunities for biodegradable magnesium alloy implants. Materials Technology. 2018; 33: 153–172. https://doi.org/10.1080/10667857.2017.1377973.

[4] He J, He FL, Li DW, Liu YL, Liu YY, Ye YJ, *et al*. Advances in Fe-based biodegradable metallic materials. RSC Advances. 2016; 6: 112819–112838. https://doi.org/10.1039/C6RA20594A.

[5] Zartner P, Cesnjevar R, Singer H, Weyand M. First successful implantation of a biodegradable metal stent into the left pulmonary artery of a preterm baby. Catheterization and Cardiovascular Interventions: Official Journal of the Society for Cardiac Angiography & Interventions. 2005; 66: 590–594. https://doi.org/10.1002/ccd.20520.

[6] Liu J, Han X, Zhang T, Tian K, Li Z, Luo F. Reactive oxygen species (ROS) scavenging biomaterials for anti-inflammatory diseases: from mechanism to therapy. Journal of Hematology & Oncology. 2023; 16: 116. https://doi.org/10.1186/s13045-023-01512-7.

[7] Wu J, Qin C, Ma J, Zhang H, Chang J, Mao L, *et al*. An immunomodulatory bioink with hollow manganese silicate nanospheres for angiogenesis. Applied Materials Today. 2021; 23: 101015. https://doi.org/10.1016/j.apmt.2021.101015.

[8] Yue F, Ayaz Z, Jiang Y, Xiang L, Huang N, Leng Y, *et al*. Dealloyed nano-porous TiCu coatings with controlled copper release for cardiovascular devices. Biomaterials Advances. 2024; 157: 213728. https://doi.org/10.1016/j.bioadv.2023.213728.

[9] Wang J, Wang Y, Xiaohalati X, Su Q, Liu J, Cai B, *et al*. A Bioinspired Manganese-Organic Framework Ameliorates Ischemic Stroke through its Intrinsic Nanozyme Activity and Upregulating Endogenous Antioxidant Enzymes. Advanced Science. 2023; 10: e2206854. https://doi.org/10.1002/advs.202206854.

[10] Tolouei R, Harrison J, Paternoster C, Turgeon S, Chevallier P, Mantovani D. The use of multiple pseudo-physiological solutions to simulate the degradation behavior of pure iron as a metallic resorbable implant: a surface-characterization study. Physical Chemistry Chemical Physics: PCCP. 2016; 18: 19637–19646. https://doi.org/10.1039/C6CP02451C.

[11] Heiden M, Walker E, Stanciu L. Magnesium, Iron and Zinc Alloys, the Trifecta of Bioresorbable Orthopaedic and Vascular Implantation-A Review. Journal of Biotechnology & Biomaterials. 2015; 5: 2. https://doi.org/10.4172/2155-952X.1000178.

[12] Gąsior G, Grodzicka M, Jędrzejewski T, Wiśniewski M, Radtke A. Comparative Study of Porous Iron Foams for Biodegradable Implants: Structural Analysis and *In Vitro* Assessment. Journal of Functional Biomaterials. 2023; 14: 293. https://doi.org/10.3390/jfb14060293.

[13] ISO. ISO 10993-5. Biological evaluation of medical devices. Part 5: Tests for *in vitro* cytotoxicity. 2009. Available at: https://www.iso.org/standard/36406.html (Accessed: 5 January 2018).

[14] ISO. ISO 10993-12. Biological evaluation of medical devices. Part 12: Sample Preparation and Reference Materials. 2021. Available at: https://www.iso.org/standard/75769.html (Accessed: 3 January 2018).

[15] Dargusch MS, Dehghan-Manshadi A, Shahbazi M, Venezuela J, Tran X, Song J, *et al*. Exploring the Role of Manganese on the Microstructure, Mechanical Properties, Biodegradability, and Biocompatibility of Porous Iron-Based Scaffolds. ACS Biomaterials Science & Engineering. 2019; 5: 1686–1702. https://doi.org/10.1021/acsbio

materials.8b01497.
[16] Goudarzi P, Moazami-Goudarzi M, Masoudi A. Sintering, microstructure and properties of absorbable Fe-Mn-xCu alloys. Materials Chemistry and Physics. 2022; 287: 126368. https://doi.org/10.1016/j.matchemphys.2022.126368.
[17] Kupková M, Hrubovčáková M, Kupka M, Oriňáková R, Morovská Turoňová A. Sintering Behaviour, Graded Microstructure and Corrosion Performance of Sintered Fe-Mn Biomaterials. International Journal of Electrochemical Science. 2015; 10: 9256–9268. https://doi.org/10.1016/S1452-3981(23)11175-8.
[18] Dehestani M, Trumble K, Wang H, Wang H, Stanciu LA. Effects of microstructure and heat treatment on mechanical properties and corrosion behavior of powder metallurgy derived Fe-30Mn alloy. Materials Science and Engineering: A. 2017; 703: 214–226. https://doi.org/10.1016/j.msea.2017.07.054.
[19] Selecka M, Bures R. Manganese in ferrous powder metallurgy. Powder Metallurgy Progress. 2001; 1: 41–58.
[20] Hryha E, Dudrova E. The Sintering Behaviour of Fe-Mn-C Powder System, Correlation between Thermodynamics and Sintering Process, Manganese Distribution and Microstructure Composition, Effect of Alloying Mode. In Mizutani, T. (ed.) Application of Thermodynamics to Biological and Materials Science (pp. 573–602). IntechOpen: London. 2011. https://doi.org/10.5772/13735.
[21] Lu X, Qin Z, Zhang Y, Wang X, Li F, Ding B, *et al*. Study of the paramagnetic-antiferromagnetic transition and the $\gamma \rightarrow \varepsilon$ martensitic transformation in Fe-Mn alloys. Journal of Materials Science. 2000; 35: 5597–5603. https://doi.org/10.1023/A:1004865331956.
[22] Şeşen FE. Practical reduction of manganese oxide. Journal of Chemical Technology and Applications. 2017; 1: 1–2. https://doi.org/10.35841/chemical-technology.1.1.26-27.
[23] Kawazoe Y, Kanomata T, Note R. MnO. In Ferreira, J.M.S., Boccaccini, A.R., Pullar, R.C. (eds.) High Pressure Materials Properties: Magnetic Properties of Oxides Under Pressure: A Supplement to Landolt-Börnstein IV/22 Series (pp. 11–16). Springer: Berlin. 2023. https://doi.org/10.1007/978-3-662-64593-2_2.
[24] Khan S, Ahmad N, Safeer A, Iqbal J. Compositional dependent morphology, structural and magnetic properties of $Fe_{100-X}Cu_X$ alloy nanowires via electrodeposition in AAO templates. Applied Physics A. 2018; 124: 678. https://doi.org/10.1007/s00339-018-2075-6.
[25] Ahmad A, Qureshi AS, Hassan A, Arshad M, Khurshid H, Mehmood U, *et al*. Synthesis of reduced graphene oxide supported FeCu and its environmental applications. Environmental Science and Pollution Research International. 2024; 31: 57655–57665. https://doi.org/10.1007/s11356-024-34965-5.
[26] Nyby C, Guo X, Saal JE, Chien SC, Gerard AY, Ke H, *et al*. Electrochemical metrics for corrosion resistant alloys. Scientific Data. 2021; 8: 58. https://doi.org/10.1038/s41597-021-00840-y.
[27] Peuster M, Hesse C, Schloo T, Fink C, Beerbaum P, von Schnakenburg C. Long-term biocompatibility of a corrodible peripheral iron stent in the porcine descending aorta. Biomaterials. 2006; 27: 4955–4962. https://doi.org/10.1016/j.biomaterials.2006.05.029.
[28] Hermawan H, Moravej M, Dubé D, Fiset M, Mantovani D. Degradation Behaviour of Metallic Biomaterials for Degradable Stents. In Chandra, T., Tsuzaki, K., Militzer, M., Ravindran C. (eds.) Advanced Materials Research (pp. 113–118). Trans Tech Publications Ltd.: Switzerland. 2007. https://doi.org/10.4028/www.scientific.net/AMR.15-17.113.
[29] Hermawan H, Alamdari H, Mantovani D, Dubé D. Iron-manganese: New class of metallic degradable biomaterials prepared by powder metallurgy. Powder Metallurgy. 2008; 51: 38–45. https://doi.org/10.1179/174329008X284868.
[30] Hermawan H, Dubé D, and Mantovani D. Development of Degradable Fe-35Mn Alloy for Biomedical Application. In Chandra, T., Tsuzaki, K., Militzer, M., Ravindran C. (eds.) Advanced Materials Research (pp. 107–112). Trans Tech Publications Ltd.: Switzerland. 2006. https://doi.org/10.4028/www.scientific.net/AMR.15-17.107.
[31] Schinhammer M, Hänzi AC, Löffler JF, Uggowitzer PJ. Design strategy for biodegradable Fe-based alloys for medical applications. Acta Biomaterialia. 2010; 6: 1705–1713. https://doi.org/10.1016/j.actbio.2009.07.039.
[32] Hermawan H, Purnama A, Dube D, Couet J, Mantovani D. Fe-Mn alloys for metallic biodegradable stents: degradation and cell viability studies. Acta Biomaterialia. 2010; 6: 1852–1860. https://doi.org/10.1016/j.actbio.2009.11.025.
[33] Moravej M, Mantovani D. Biodegradable metals for cardiovascular stent application: interests and new opportunities. International Journal of Molecular Sciences. 2011; 12: 4250–4270. https://doi.org/10.3390/ijms12074250.
[34] Scarcello E, Lison D. Are Fe-Based Stenting Materials Biocompatible? A Critical Review of *In Vitro* and *In Vivo* Studies. Journal of Functional Biomaterials. 2019; 11: 2. https://doi.org/10.3390/jfb11010002.
[35] Zhao Y, Zang G, Yin T, Ma X, Zhou L, Wu L, *et al*. A novel mechanism of inhibiting in-stent restenosis with arsenic trioxide drug-eluting stent: Enhancing contractile phenotype of vascular smooth muscle cells via YAP pathway. Bioactive Materials. 2020; 6: 375–385. https://doi.org/10.1016/j.bioactmat.2020.08.018.
[36] Ceylan H, Tekinay AB, Guler MO. Selective adhesion and growth of vascular endothelial cells on bioactive peptide nanofiber functionalized stainless steel surface. Biomaterials. 2011; 32: 8797–8805. https://doi.org/10.1016/j.biomaterials.2011.08.018.
[37] Yau JW, Teoh H, Verma S. Endothelial cell control of thrombosis. BMC Cardiovascular Disorders. 2015; 15: 130. https://doi.org/10.1186/s12872-015-0124-z.
[38] Thrivikraman G, Madras G, Basu B. *In vitro/In vivo* assessment and mechanisms of toxicity of bioceramic materials and its wear particulates. RSC Advances. 2014; 4: 12763–12781. https://doi.org/10.1039/C3RA44483J.
[39] Furuhashi A, Ayukawa Y, Atsuta I, Okawachi H, Koyano K. The difference of fibroblast behavior on titanium substrata with different surface characteristics. Odontology/the Society of the Nippon Dental University. 2012; 100: 199–205. https://doi.org/10.1007/s10266-011-0029-y.
[40] King D, McCormick C, McGinty S. How Does Fluid Flow Influence Drug Release from Drug Filled Implants? Pharmaceutical Research. 2022; 39: 25–40. https://doi.org/10.1007/s11095-021-03127-4.
[41] Yan F, Li K, Xing W, Dong M, Yi M, Zhang H. Role of Iron-Related Oxidative Stress and Mitochondrial Dysfunction in Cardiovascular Diseases. Oxidative Medicine and Cellular Longevity. 2022; 2022: 5124553. https://doi.org/10.1155/2022/5124553.
[42] Zhang Y, Roux C, Rouchaud A, Meddahi-Pellé A, Gueguen V, Mangeney C, *et al*. Recent advances in Fe-based bioresorbable stents: Materials design and biosafety. Bioactive Materials. 2023; 31: 333–354. https://doi.org/10.1016/j.bioactmat.2023.07.024.
[43] Ochijewicz D, Tomaniak M, Opolski G, Kochman J. Inflammation as a determinant of healing response after coronary stent implantation. The International Journal of Cardiovascular Imaging. 2021; 37: 791–801. https://doi.org/10.1007/s10554-020-02073-3.
[44] Cornelissen A, Vogt FJ. The effects of stenting on coronary endothelium from a molecular biological view: Time for improvement? Journal of Cellular and Molecular Medicine. 2019; 23: 39–46. https://doi.org/10.1111/jcmm.13936.
[45] Zhang X, Tian X, Wang Y, Yan Y, Wang Y, Su M, *et al*. Application of lipopolysaccharide in establishing inflammatory models. International Journal of Biological Macromolecules. 2024; 279: 135371. https://doi.org/10.1016/j.ijbiomac.2024.135371.
[46] Díez-Tercero L, Delgado LM, Bosch-Rué E, Perez RA. Evaluation of the immunomodulatory effects of cobalt, copper and magnesium ions in a pro inflammatory environment. Scientific Reports. 2021; 11: 11707. https://doi.org/10.1038/s41598-021-91070-0.
[47] Tu Z, Zhong Y, Hu H, Shao D, Haag R, Schirner M, *et al*. Design of therapeutic biomaterials to control inflammation. Nature

Reviews. Materials. 2022; 7: 557–574. https://doi.org/10.1038/s41578-022-00426-z.

[48] Díez-Tercero L, Delgado LM, Bosch-Rué E, Perez RA. Evaluation of the immunomodulatory effects of cobalt, copper and magnesium ions in a pro inflammatory environment. Scientific Reports. 2021; 11: 11707. https://doi.org/10.1038/s41598-021-91070-0.

[49] Feldman D. The Effect of Size of Materials Formed or Implanted *In Vivo* on the Macrophage Response and the Resultant Influence on Clinical Outcome. Materials. 2021; 14: 4572. https://doi.org/10.3390/ma14164572.

[50] Amani H, Alipour M, Shahriari E, Taboas JM. Immunomodulatory Biomaterials: Tailoring Surface Properties to Mitigate Foreign Body Reaction and Enhance Tissue Regeneration. Advanced Healthcare Materials. 2024; 13: e2401253. https://doi.org/10.1002/adhm.202401253.

Editor's note: The Scientific Editor responsible for this paper was Yang Liu.

Received: 2nd April 2025; **Accepted**: 9th September 2025; **Published**: 31st December 2025